Hollow penetration electrode of Bi with dislocated lattice enabling ampere-level reduction of CO_2 exclusively to formate

Aohui Chen [a,b,c], Chang Zhu [a,b], Jianing Mao [b,d], Shoujie Li [a], Gangfeng Wu [a,b], Yiheng Wei [a,b], Xiaohu Liu [a,b,c], Xiao Dong [a], Yanfang Song [a,b], Guihua Li [a,b], Yuhan Sun [c,*], Wei Wei [a,b,c,**], Wei Chen [a,b,**]

[a] *CAS Key Laboratory of Low-Carbon Conversion Science and Engineering, Shanghai Advanced Research Institute, Chinese Academy of Sciences, Shanghai 201210, PR China*
[b] *University of the Chinese Academy of Sciences, Beijing 100049, PR China*
[c] *School of Physical Science and Technology, ShanghaiTech University, Shanghai 201210, PR China*
[d] *Shanghai Institute of Applied Physics, Chinese Academy of Sciences, Shanghai 201204, PR China*

ARTICLE INFO

ABSTRACT

CO_2 electroreduction to valuable chemicals using renewable energy is a prospective strategy for realizing carbon neutrality, however, exclusive production of formate under high industry current densities (> 200 mA cm^{-2}) remains challenging. Herein, we presented a lattice-dislocated hollow-fiber Bi via in situ reconstruction to make a breakthrough for such issue. A nearly perfect formate Faradaic efficiency of > 99.5 % was realized with a current density of 1 A cm^{-2}, completely suppressing CO and hydrogen generation. Finite element simulations showed high-concentration CO_2 feeding was realized even though at ampere-level current density. And density functional theory calculations revealed that the abundant dislocated lattice acting as the active sites boosted the production of OCHO* . Thus, the synergistic combination of penetration and strain effects induced by the lattice-dislocated Bi hollow penetration electrode is responsible for such remarkable activities. This work represents a large step toward the application of direct conversion of CO_2.

1. Introduction

Electrochemical reduction of carbon dioxide (CO_2) to value-added fuels powered by clean energy has considerable potential for mitigating the greenhouse effect [1–3]. Therefore, tremendous research works have been done to convert CO_2 into renewable chemical fuels, such as C_1 products (CH_4, CO, CH_3OH, and HCOOH) [4–7] and C_2 products (C_2H_5OH, CH_3COOH, C_2H_4, C_2H_6, and n-propanol) [8–11]. Among these products, the formate product is regarded as the most profitable per mole of electrons according to the recent technoeconomic analyses [12–14]. In addition, formic acid is highly desirable owing to its various advantages such as easy availability, preservation, high energy density, and low toxicity [15–17]. Hence, exploring stable and exclusive catalysts under industry-level current density (>200 mAcm^{-2}) for forming a formate product is urgent and essential.

Over the past years, several IIIA, IVA, and VA metals (i.e., In, Sn, Pb,

and Bi) have been selected for their high selectivity to form formate product [18–21]. Among these metals, metallic Bi stands out for use in electrochemical CO_2 reduction reaction (eCO2RR) owing to its low toxicity and cost. To date, numerous studies have achieved high Faradaic efficiency or high current density for the CO2RR based on Bi-based catalysts [22–26]. However, the current research is predominantly plagued by the following problems. On the one hand, some reported studies have achieved exclusive selectivity, but have delivered insufficient current density [27–29]. There are because of the limited gaseous reactant mass transport and the presence of a thick gaseous reactant diffusion boundary layer in traditional planar electrodes [30]. On the other hand, although ampere-level CO_2 reduction for formate product generation was realized, a Faradaic efficiency of only ~95 % was achieved (Table S1) [31,32]. Thus, ampere-level and exclusive CO_2 reduction remains a formidable challenge.

Hollow penetration electrodes (HPEs) with hierarchical pore

structures show promising benefits for conversion of CO_2 [33–36]. These electrodes compel the gas to penetrate through hollow fiber wall and then the gas arrives at the catalyst layer rather than being diffused in the planar electrode. As a result, the steady and sufficient reactants remained at triphasic reaction interfaces in this hollow-fiber (HF) configurations [32]. Furthermore, the self-supported electrode with well-integrated porous structure comprised a solitary metallic component without any additives and binders, thereby preventing flood efficiently and exhibiting boosted structural stability [37]. Hence, the penetration electrode could achieve sufficient CO_2 supply and facilitate CO_2 reduction reaction kinetics at ampere-level current density. Furthermore, surface structure modulations are regarded as an exquisite strategy to promote catalytic activity by regulating the adsorption free energy of key reaction intermediates [38–41], which determines the formation of final products. Recently, we have achieved efficient reduction of CO_2 to form valuable chemicals at large current density (>1 A cm^{-2}) by designing the surface structure of metal HFs [32,42–44].

Inspired by these advantages, herein, we report the development of lattice-dislocated Bi with abundant nanosheets for use as an HPE. For such D-Bi HPEs, the gaseous reactants are compelled to penetrate through the highly porous hollow-fiber walls and then are fed continuously to the surface of active D-Bi nanosheets (Scheme 1). Moreover, geometric phase analysis (GPA) images of the Bi (012) plane over D-Bi HF and density functional theory (DFT) calculations demonstrated that the strain effect induced by the dislocated lattice could reduce the activation energy barriers for the HCOO* formation, thereby boosting reduction reaction kinetics while inhibiting the hydrogen evolution reaction (HER) (Scheme 1). In hence, CO_2 was exclusively converted to formate with a nearly perfect Faradaic efficiency of > 99.5 % at the ampere-level current density while completely suppressing the formation of CO and H_2. Thus, the current study exhibits significant potential for the renewable utilization of CO_2.

2. Experimental

2.1. Materials

Bi_2O_3 powder (99 % purity, 300 nm) was purchased from Shanghai Xiangtian Nano Materials Co., Ltd, Polyetherimide (PEI) from Saudi Basic Industries Corporation (SABIC). Nafion 117 membrane was purchased from DuPont. N-methyl-2-pyrrolidone (NMP) and Potassium chloride (KCl) were purchased from Sinopharm Chemical Reagent Co., Ltd. 3-Trimethylsilyl-1-propane sulfonic acid sodium salt (DSS) was purchased from Tokyo Chemical Industry Co., Ltd, Deuterium oxide

(D_2O) was purchased from Sigma-Aldrich. All chemicals were used as received without further purification. Electrolyte solutions were prepared using 18.2 MΩ H_2O (Master-S30UVF water purification system).

2.2. Preparation of Bi and D-Bi

2.2.1. Preparation of Bi hollow fiber

The Bi hollow fiber was obtained from the chemical reduction of Bi_2O_3 HF in 0.5 M $NaBH_4$ solution (0.1 M NaOH) for 3 h. Bi_2O_3 HF was synthesised via a combined phase-inversion/sintering process (Fig. S1), explained elsewhere [32]. In brief, homogeneous and transparent solution of PEI (20 g), NMP (70 g) and Bi_2O_3 powder (110 g) was prepared. Then, the mixture was extruded by the spinning machine and shaped in the tap water bath obtain Bi_2O_3 hollow-fiber green body. Next, the Bi_2O_3 hollow-fiber green body was sintered in air flow (100 mL min^{-1}) at 550 °C (heating rate: 1 °C min^{-1}) for 6 h and then partly reduced in hydrogen flow (100 mL min^{-1}) at 250 °C (heating rate: 3 °C min^{-1}) for 12 h. Sequently, as-formed hollow-fiber Bi/Bi_2O_3 was futher sintered in Ar flow (100 mL min^{-1}) at 720 °C (heating rate: 1 °C min^{-1}) for 6 h to obtain tough hollow-fiber framework and the as-obtained hollow-fiber framework was calcined once more in air flow (100 mL min^{-1}) at 500 °C (heating rate: 1 °C min^{-1}) for 4 h to get pure Bi_2O_3 HF.

2.2.2. Preparation of D-Bi hollow fiber

D-Bi HF was abtained from the electrochemical redox of Bi HF. First, the Bi HF was electrochemical oxidation at a fixed potential of 0.7 V (vs. RHE) for 30 s and then reduction at -3.0 V for 30 min. The exposed geometric area of working electrode (D-Bi HF) was about 0.36 cm^2 ($S=n\pi D_{out}L=1 \times 3.14 \times 380 \times 10^{-4} \times 3 = 0.36$ cm^2).

2.3. Materials characterization

The cross-section and surface of hollow fiber were inspected by scanning electron microscope (SEM) (JSM-7800). The crystalline phases of Bi HF and D-Bi HF catalysts were characterized by X-ray diffraction (XRD) on a Bruker D8 Advance using Cu Kα source ($\lambda = 1.54$ Å). The high-resolution images were acquired from a cold FEG JEOL Grand-ARM 300 F (JEOL, Tokyo, Japan) operated at 300 kV. The quantification detection of formate product was from Bruker Avance III HD500. For N_2 adsorption, the standard degassing station of the Mack instrument was used, and the samples were pretreated under the condition of vacuum 300 ℃ for 7 h, and then the samples were tested for nitrogen adsorption and desorption under the condition of 77 K liquid nitrogen using a
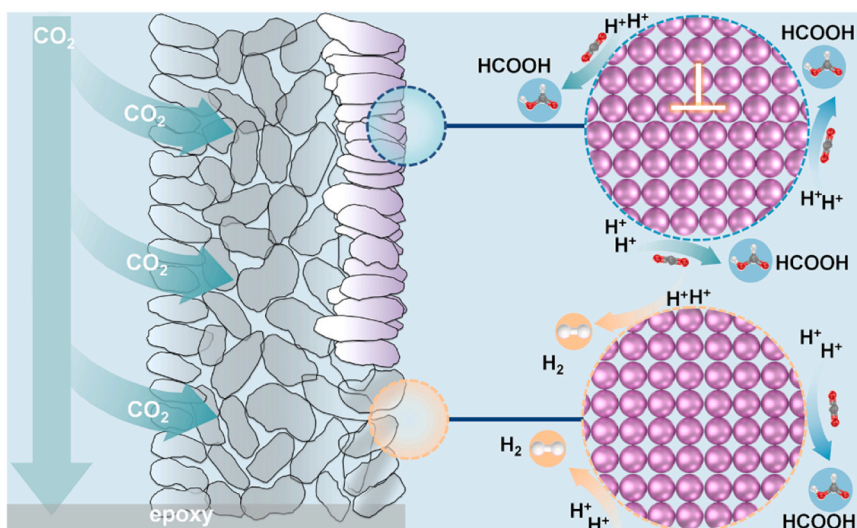
Scheme 1. Diagrammatic representation of lattice-dislocated bismuth for exclusive CO_2 electroreduction to formate.

Quantachrome Autosorb IQ3 automatic specific surface area analyzer. The inductively coupled plasma optical emission spectrometry (ICP-OES) tests were performed on a Thermo Fisher iCAP PRO with a 0.02 ppm detection limit for Bi^{3+} using RF Power under 1150 W, a plasma flow of 0.5 L min^{-1}, an auxiliary flow of 0.5 L min^{-1}, a nebulizer flow of 12.5 L min^{-1}, and a sample uptake delay of 30 s

2.4. Electrocatalytic reduction of CO_2

The electrochemical CO_2 reduction reaction were performed at homemade H-type electrolysis cell under ambient conditions on the Biologic VMP3 potentiostat. The cathodic and anodic compartments were separated by a Nafion 117 membrane, and a KCl-saturated Ag/AgCl was regarded as reference electrode and a platinum mesh counter was counter electrode. Actually, the 3 M $KHCO_3$ was used as the anolyte and 3 M KCl was used as the catholyte in this work, respectively. And anolyte and catholyte separated by the nafion membrane were cycled and refreshed at the same fixed flow rate of 30 mL min^{-1} by using two identical peristaltic pumps (Jihpump BT-50EA 153YX), respectively. The CO_2 flow rate was fixed at 10 mL min^{-1} during CO_2 electro-reduction reaction unless otherwise stated.

2.5. Product quantifications

Gas-phase products produced in the cathode chamber during the electrochemical reaction directly enter the gas chromatograph (GC-2014, Shimadzu) equipped with a Molecular sieve-13 $\times$ 60/80 column and a Plot-Q80/100 column using flame ionization detector (FID) during the electrochemical reactions and analysed online, the product H_2 from the cathode compartment was also analysed using a thermal conductivity detector (TCD). A GC run was initiated every 15 min. High purity nitrogen (99.999 %) was used as the carrier gas. In all the potentiostat electrolysis tests only H_2 and CO were found to be gas-phase products. The faradaic efficiency (FE) of products was calculated by following Eq. (1):

$$FE = \frac{C_{product} \times 10^{-6} \times \nu_{CO_2} \times 10^{-3} \times t \times \alpha \times 96485}{22.4 \times Q} \times 100\% \quad (1)$$

Hence,

$C_{product}$ is the concentration of the gas-phase products, ppm.

v is the flow rate of CO_2, mL min^{-1}.

α is the number of electrons transferred from CO_2 to products.

t is the reaction time, s.

Q is the total quantity of electric charge, A s.

Liquid phase products from the cathode compartment after each potentiostatic electrolysis experiment for 30 min were analysed using a 600 MHz NMR spectrometer (Bruker), with DSS and D_2O as internal standards. After 30 min electrochemical reduction, electrolyte solution (0.5 mL) containing liquid products of electrical reduction was mixed with 0.1 mL 3-Trimethylsilyl-1-propane sulfonic acid sodium salt (DSS, Tokyo Chemical Industry Co.) (6 mM) and 0.1 mL deuterium oxide (D_2O, Sigma-Aldrich) for use as internal standards. The FE of liquid products was calculated by following Eq. (2):

$$FE = \frac{C_{product} \times 10^{-6} \times V \times \rho_{product} \times n \times 96485}{M_{product} \times Q} \times 100\% \quad (2)$$

Hence,

C is the concentration of formic acid, ppm.

V is the liquid volume in the cathode chamber, mL.

ρ is the density of formic acid, g mL^{-1}.

n is the number of electrons transferred from CO_2 to products formic acid.

M is the molecular weight of formic acid, g mol^{-1}.

Q is the total quantity of electric charge, A s.

The theoretical limits of formate partial current density, i.e., $j_{formate,}$ lim(gas) and $j_{formate,lim(sol)}$ were calculated by the following two Eqs. (3) and (4), respectively. The former $j_{formate,lim(gas)}$ is the theoretical limit of formate partial current density with all gas-phase CO_2 molecules inputted into the electrolysis cell were electroreduced to formate. The latter $j_{formate,lim(sol)}$ is the theoretical limit of formate partial current density with all CO_2 molecules dissolved in the electrolyte solution were electroreduced to formate.

$$j_{formate,lim(gas)} = \frac{nF\nu_{CO_2}}{S_{HF}V_m} \quad (3)$$

$$j_{formate,lim(sol)} = nFD\frac{C}{\delta} \quad (4)$$

where n is the number of transferred electrons for producing formate.

F is the Faraday constant, 96485 C•mol^{-1}.

S is the electrode area, cm^2.

ν_{CO2} is the flow rate of CO_2, mL min^{-1}.

V_m is the gas mole volume, (24.5 L mol^{-1} at 25 °C, 101.325 kPa).

D is the diffusion coefficient of CO_2, m^2 s^{-1}.

c is the saturated bulk concentration of CO_2, mol L^{-1}.

δ is the diffusion layer thickness.

3. Results and discussion

3.1. Preparation and structural characterizations

Bi HF was prepared via wetting chemical reduction of Bi_2O_3 HF, followed by in situ electrochemical redox treatment to obtain the lattice-dislocated Bi (D-Bi) HF (Fig. 1a). Through the cross-section view of the Bi_2O_3 HF (Fig. 1b), typical scanning electron microscopy images displayed that Bi_2O_3 HF showed unique finger-like void structures, which was prepared via phase inversion and calcinating processes (Fig. S1). In addition, molten Bi_2O_3 particles instead of dispersive globular particles in the raw green body (Fig. S2) composed the well-integrated outer surface of Bi_2O_3 HF (Fig. 1c), indicating the presence of tough porous self-supported framework structures that were obtained via calcination during the fabrication of Bi_2O_3 HF. However, in comparison to the outer surface of Bi_2O_3 HF (Fig. 1c), chemical reduction showed no discernible influence on the Bi HF outside surface (Fig. 1d). Subsequently, unlike the smooth surface of Bi_2O_3 HF and Bi HF, plenty of nanosheets appeared the D-Bi HF outside surface (Fig. 1e and Fig. S3) after the in situ electrochemical redox treatment. Furthermore, N_2 adsorption and desorption measurements were carried out to obtain the pore sizes and pore distributions of D-Bi HF and Bi HF, which were based on BJH method adsorption pore diameter. Both D-Bi HF and Bi HF showed narrow pore distributions (Fig. S4), and their average pore sizes were 5.55 nm and 7.06 nm, respectively. The BET specific surface areas of D-Bi HF and Bi HF were 19.22 m^2/g and 12.6 m^2/g, respectively (Table S2), implying the rougher surface of D-Bi HF, as evidenced by the SEM observations (Figs. 1d and 1e). Moreover, the characteristic peaks of Bi_2O_3 disappeared and the characteristic peaks of metallic Bi appeared in the X-ray diffraction (XRD) patterns (Fig. 1f), indicating the transition of the residual Bi_2O_3 to metallic Bi as well as the total formation of metallic Bi during the wetting chemical reduction and in situ electrochemical redox treatment. Besides, Raman spectra (Fig. S5) and X-ray photoelectron spectroscopy (XPS) (Fig. S6) also demonstrated that the hollow-fiber Bi bulk and surface structures were both same as pure metallic bismuth [24,45], corresponding to the XRD results (Fig. 1F). Furthermore, the representative spherical aberration-corrected high-resolution high-angle annular dark-field scanning transmission electron microscopy (HAADF–STEM) images exhibited a well-organized lattice for Bi HF (Fig. 1g) and D-Bi HF (Fig. 1h), indicating the comparative perfect crystalline structure of these samples. In addition, a lattice spacing of 3.2 Å corresponding to Bi (012) plane were observed for Bi HF. However, a lattice spacing of 3.4 Å was observed in some regions of the D-Bi HF samples, which is slightly larger than the ideal crystal lattice size of
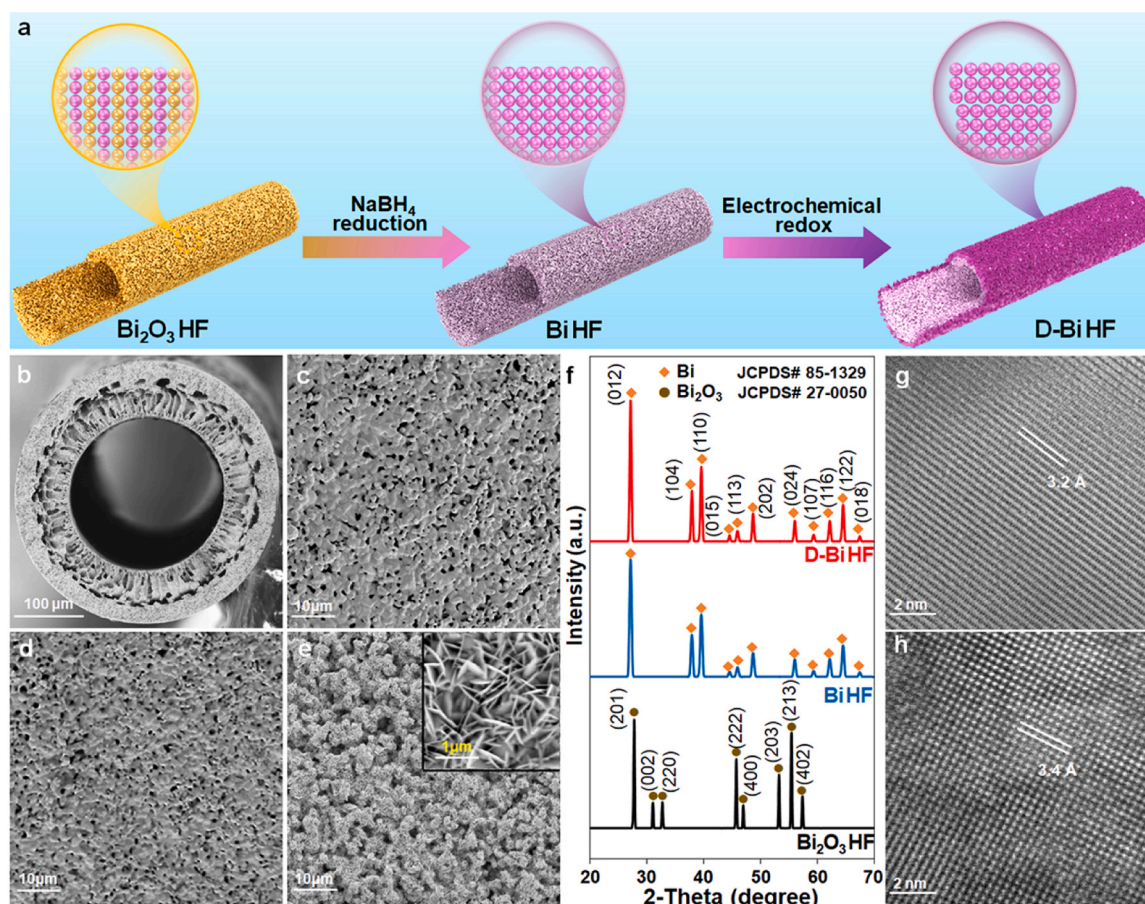
Fig. 1. (a) Diagrammatic representation of synthesis for D-Bi. SEM images of (b) Bi_2O_3 HF cross-section, (c) Bi_2O_3 HF outside surface, (d) Bi HF outside surface and (e) D-Bi HF outside surface with the low magnification and (inset) the high magnification. (f) XRD patterns. HAADF-STEM images of (g) Bi HF and (h) D-Bi HF. The lattice spacings of 3.2 Å and 3.4 Å in (g) and (h) corresponds to the Bi (012) planes of Bi HF and D-Bi HF, respectively.

3.2 Å [46]. This is most likely due to several structural defects in the D-Bi HF.

To gain a better understanding of the defects, the HAADF–STEM image of D-Bi was analyzed in greater detail (Fig. 2a and b). Fig. 2c depicts the inverse fast Fourier transform images of Fig. 2b, which are associated with the Bi (012) plane. The locations marked with "T" represent dislocations. Notably, a lattice spacing of 3.4 Å was observed in the "T" region, corresponding to the square area in the Fig. 2c, which displayed about ~6 % plane expansion [47]. The result suggests that the variation in lattice spacing was caused by dislocations, that is the presence of extra the half-atomic plane during the dislocation on the surface caused the distortion of the surrounding lattice space of the D-Bi nanosheets, resulting in the expansion of the lattice space in the regions. In addition, Fig. 2d–f depict the GPA images of the Bi (012) plane shown in Fig. 2b and c. As indicated by the strain distribution in Fig. 2d–f, it can be concluded that the principal cause of lattice changes was attributable to the strain effects induced by dislocations on the (012) plane. The probably reason for generate dislocated lattice is that the intermediate BiO_xCl_y species might form during the electrochemical oxidation, and the rapid release of non-metallic elements occurred at the large negative potential − 3.0 V to obtain metallic Bi HF. Then, kinds of atoms displayed different surface diffusion during the redox processes, which caused the formation of dislocated lattice, in consistence with the previous reports [46,48,49].

3.2. Electrocatalytic CO₂RR performance

A D-Bi HPE was served as the working electrode to estimate the catalytic performance for the CO₂RR in home-made H-type flow cell (Fig. S7) system under ambient conditions. The 3 M KHCO₃ was used as the anolyte and 3 M KCl was used as the catholyte in this work, respectively. And anolyte and catholyte were separated by the nafion membrane to avoid the formation of Cl₂ or HClO [50]. Furthermore, to verify the structural superiority of D-Bi HF, D-Bi HF with non-penetrating mode (npD-Bi HF) and Bi HF were also fabricated for comparison. Fig. 3a shows the distribution of different products as their FEs for formate in 3 M KCl at the applied potentials ranging from − 0.65 to − 0.98 V (vs. RHE). The H₂ FE is always lower than 0.5 %; however, the formate FE showed a slight decrease from 100 % to 99.5 % (Fig. 3a and S8, Table S3), and the H₂ FE increased slightly to 6 % as the potential increased to − 1.05 V (Fig. S8, Table S3). Moreover, the CO FE was completely suppressed at applied potentials ranging from − 0.65 to − 1.05 V (Fig. S8, Table S3). Furthermore, $j_{formate}$ reached 1010 mA cm^{-2} with a near-perfect Faradaic efficiency of > 99.5 % at − 0.98 V over D-Bi HF (Fig. 3b and S9, Table S3), surpassing the previous prominent catalysts (Table S1). However, compared with D-Bi HF, npD-Bi HF exhibited inferior catalytic performance with predominant hydrogen evolution (Fig. 3a and S10), whereas superior catalytic performance was achieved in for D-Bi HF under the same potential. This result reveals that the CO₂ reduction reaction kinetics were indeed confined by the limited mass transport. Moreover, Bi HF also exhibited a significant ability to convert CO₂ to formate, however, their FE_{formate} values were ~70 % of those of D-Bi HF (Figs. 3a, S9, and S11, Table S3), indicating that the strain effects induced by a dislocated lattice may play a key role in for the formate product formation. The electrochemically active surface areas (ECSAs) of D-Bi HF and Bi HF were determined by
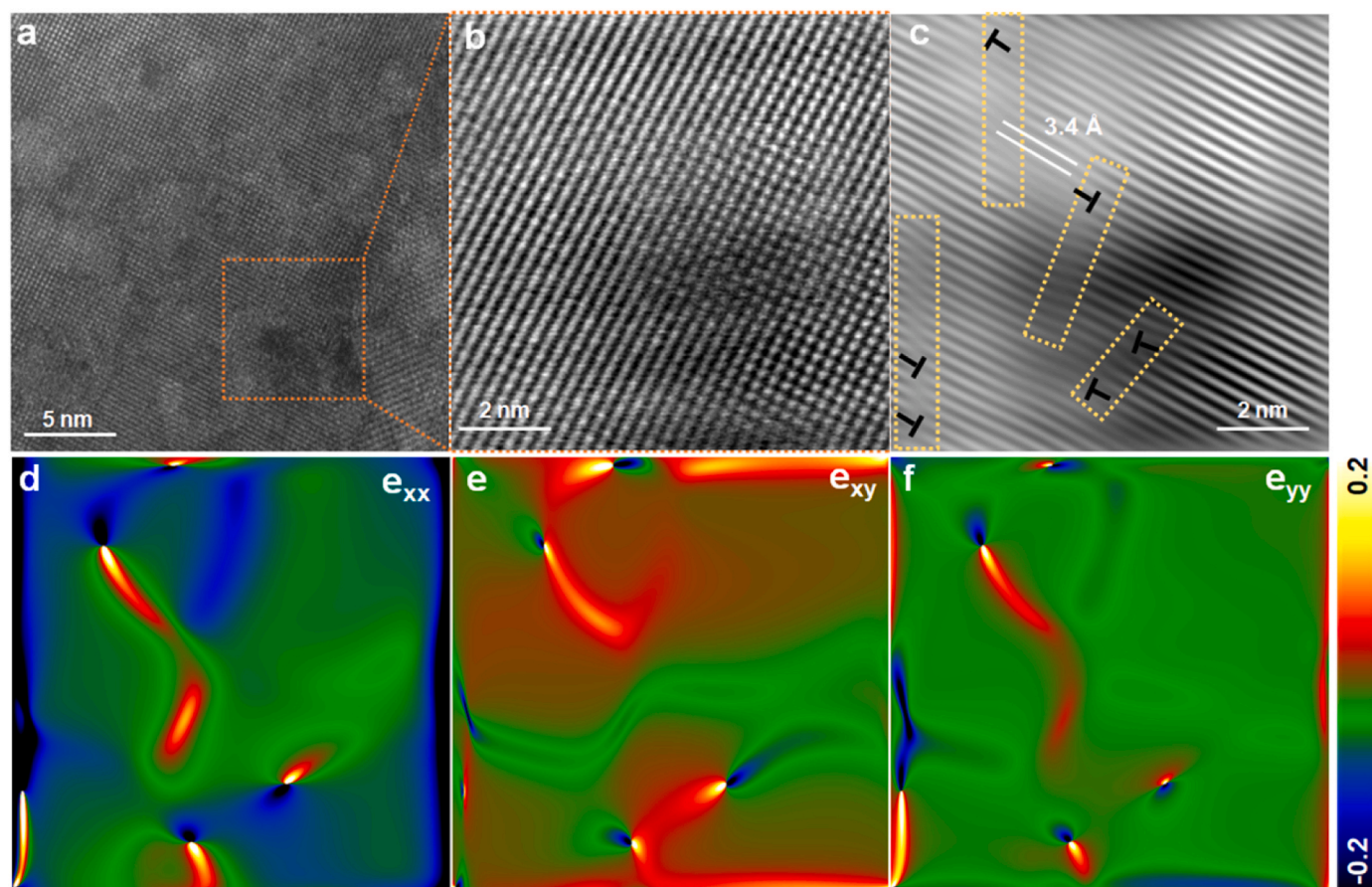
Fig. 2. Structural characterization of D-Bi HF. HAADF-STEM images of (a) D-Bi HF and (b) enlarged areas corresponding to the square area in (a). (c) IFFT patterns of (012) plane of the D-Bi, corresponding to the square area in (a), showing dislocations marked with "T". Strain distributions of (d) e_{xx}, (e) e_{xy} and (f) e_{yy}.
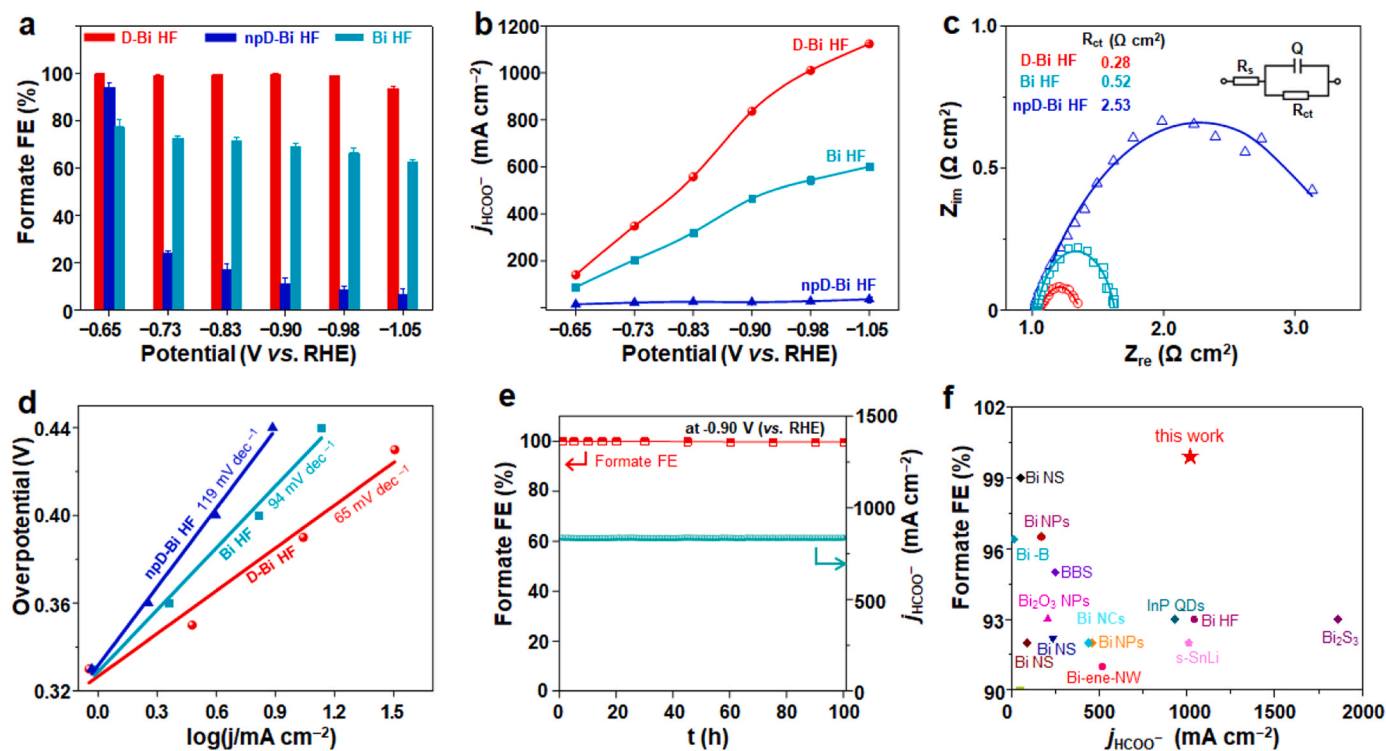

Fig. 3. (a) FE, (b) Formate current densities and (c) Nyquist plots at − 0.98 V for npD-Bi HF, D-Bi HF and Bi HF. (d) Tafel slopes of D-Bi HF, npD-Bi HF and Bi HF. (e) Long-term performance test at − 0.90 V. (f) Performance comparisons with reported prominent electrocatalysts.

measuring their double-layer capacitance (C_{dl}) values via their cyclic voltammetry (CV) curves (Fig. S12). The ECSA of D-Bi HF was 23 mF cm^{-2}, larger than that of Bi HF (16 mF cm^{-2}). Electrochemical impedance spectroscopy was carried out to research the electron transfer behaviors of all samples. Fig. 3c showed that the D-Bi HF had the lowest charge transfer resistance (R_{ct}) (0.28 Ω cm^{-2}) compared with npD-Bi HF (2.53 Ω cm^{-2}) and Bi HF (0.52 Ω cm^{-2}). Those results demonstrated that D-Bi HF were superior to npD-Bi HF and Bi HF electrodes in terms of electrical conductivity, indicating that D-Bi HF with plenty of nanosheets boosts the charge-transfer process [51]. Furthermore, the Tafel analysis and the comparison were conducted for D-Bi HF, npD-Bi HF and Bi HF. Since CO and H$_2$ amount formed over D-Bi HF were negligible at all potentials, the Tafel analyses for CO and H$_2$ over D-Bi HF were not carried out. While the Tafel slopes for both CO (230 mV dec^{-1}) and H$_2$ (101 mV dec^{-1}) over Bi HF were smaller than for CO (250 mV dec^{-1}) and H$_2$ (129 mV dec^{-1}) over npD-Bi HF (Fig. S13). Note that the Tafel slope

for HCOO$^-$ formation over D-Bi HF yielded the smallest value of 65 mV dec^{-1} compared to those over npD-Bi HF (119 mV dec^{-1}) and Bi HF (94 mV dec^{-1}), as shown in Fig. 3d, implying the best reaction kinetic in D-Bi HF [52–54]. Moreover, linear sweep voltammetry (LSV) and cyclic voltammetry (CV) curves of D-Bi HF, npD-Bi HF and Bi HF showed that the same negligible current densities appeared in the potential range from − 0.25 to − 0.55 V, after which their current densities increased rapidly as the applied potential negatively shifted from − 0.55 to − 1.94 V (Fig. S14). And D-Bi HF had the largest current densities during the potential window compared to npD-Bi HF and Bi HF (Fig. S14), which resulted from the best reaction kinetics in D-Bi HF.

Further evaluation of the durability of D-Bi HF was conducted at − 0.90 V, where the formate FE remained > 99 % and the total current densities remained constant at 840 mA cm^{-2}, showing no sign of deterioration after 100 h of electrolysis (Fig. 3e). While the corresponding potentials against time were fluctuant to some degree, as shown in
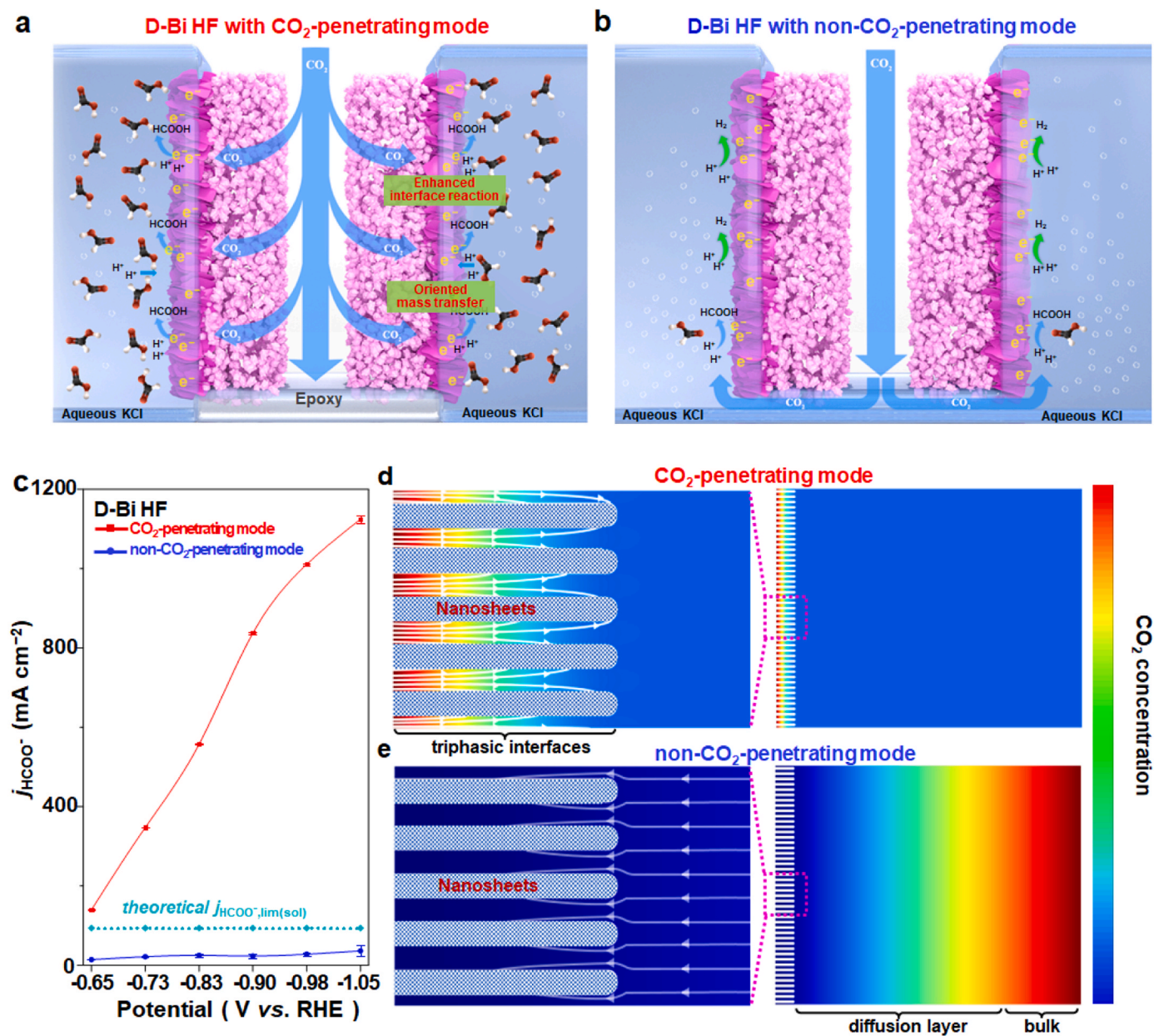
Fig. 4. (a) CO$_2$-penetrating and (b) non-CO$_2$-penetrating modes for D-Bi HF. c Formate partial current densities (j$_{formate}$) of CO$_2$-penetrating and non-CO$_2$-penetrating modes for D-Bi HF. Finite element simulations based on COMSOL Multiphysics. CO$_2$ concentration distribution of (d) CO$_2$-penetrating and (e) non-CO$_2$-penetrating modes for D-Bi HF. Arrows in (d) and (e) show the direction of CO$_2$ stream/diffusion.

Fig. S15. The result was one of the highest reported selectivity under ampere-level current density (Fig. 3f). In addition, the ICP-OES measurements of the outlet electrolyte indicated that no Bi dissolution was found under the eCO_2RR conditions (Table S4). Moreover, the post-reaction XRD for D-Bi HF also demonstrated that the D-Bi HF structure was same as that before reaction (Fig. S16), and the surface nanosheets were also same as that of the initial D-Bi HF (Fig. S17), indicating structural stability of D-Bi HF. In addition, the postreaction HAADF–STEM image revealed that the dislocated lattice was stable after 100 h of electrolysis (Fig. S18). Furthermore, this structure could avoid flooding compared with GDEs, being responsible for the stable and superior catalytic activity for D-Bi HF.

3.3. CO₂ penetration effect

The electrocatalytic reaction under large current densities demands enough feeding of CO_2 molecule in CO_2 electroreduction. D-Bi HF provided a scene where CO_2 molecule was highly dispersed and forcibly interacted with active sites, thus achieving local pretty ample CO_2 at the active sites to satisfy high-speed formate production rate (Fig. 4a), thus breaking the limitation of low CO_2 solubility in aqueous solutions. Furthermore, penetration direction of CO_2 molecule from interior to exterior promoted the departures of formate product, avoiding efficiently any possible delay or accumulation. In conjunction with well-integrated micro/nanostructures, the abovementioned two advantages favor the entire CO_2 reduction kinetics, resulting in the lowest charge transfer resistance (($0.28\ \Omega\ cm^{-2}$)). Conversely, the non-CO_2-penetrating manner completely lost the abovementioned advantages, i.e., compulsive interactions with triphasic sites and directional mass transports, despite preserving the same hierarchical structures (Fig. 4b). Thus, the ultrahigh $j_{formate}$ values were realized when using Bi HF in CO_2-penetrating manner, outperforming a theoretical limit value of $\sim$94 mA cm^{-2} [55], in the light of the 100 % conversion of dissolved CO_2 in electrolytes with a saturated concentration of 34 mM. Notably, D-Bi HF exhibited low $j_{formate}$ values, with a maximum $j_{formate}$ value of 36 mA cm^{-2} at − 1.05 V (Fig. 4c), indicating that the reaction kinetics were indeed constrained by limited CO_2 feeding.

To gain in-depth insight on the CO_2 penetrating effect over D-Bi HF, considering the combination of the mass transfer kinetics and electrode–electrolyte interactions is crucial, which are modeled using the Butler–Volmer equation and diffusion system [56], respectively. Therefore, finite element simulations based on COMSOL Multiphysics® were conducted to describe the CO_2 concentration distributions over D-Bi HF in both CO_2-penetrating and non-CO_2-penetrating modes. The two-dimensional model depicted in Fig. 4d and e consists of both penetrating microchannel structures in the outer wall of HF and the diffusion layer/bulk in the electrolyte. The simulation results revealed that the continuous CO_2 stream compulsively rushed out of the micropores of the HF wall and arrived at the electro-reaction regions on the outer surface of the penetration electrode containing abundant active Bi nanosheets. Admittedly, the thickness of the diffusion layer was drastically reduced, which contributed to the maintenance of an exceptionally high local CO_2 concentration at triphasic interfaces for its highly efficient.

CO_2 electroreduction performance (Fig. 4d). By contrast, for non-CO_2-penetrating mode of D-Bi HF (Fig. 4d), the CO_2 reactant on the electrode surface was primarily derived from the diffusion of the dissolved CO_2 molecule in bulk electrolyte [57,58], resulting in an extremely low CO_2 concentration in their electro-reaction regions.

3.4. Strain effects

DFT calculations were performed to investigate further how the strain effects of the D-Bi HF electrode enhance the CO_2RR performance. The crucial intermediate HCOO* for formate production was detected via in situ attenuated total reflectance-Fourier transform infrared (ATR-

FTIR) (Fig. 5a) [59]. Moreover, CO_3^{2-} appeared with simultaneous b-CO_3^{2-} group at 1470 cm^{-1} [60], the broad peak at 1560 cm^{-1} could be assigned to the HCOO$^-$ [61,62]. As shown in Fig. 5b, we constructed the Bi (012) models with strain effects of − 6 %, 0 %, and 6 % to evaluate the capability of generating HCOO* intermediate under different strain effects over D-Bi HF, denoted as Bi (0.94), Bi (1.00), and Bi (1.06) (Fig. S19), respectively. Both the optimized adsorption structures and adsorption energies of H* , CO_2 * , HCOO* , and HCOOH* intermediates are depicted in Fig. 5b and Fig. S20. As observed, the free energy for the HCOO* formation via the first proton-electron transfer was 1.15, 0.96, and 0.96 eV, respectively, for strain effects of − 6 %, 0 %, and 6 %. Moreover, the free energy for *H formation was 1.04 eV over the surface of Bi (1.06), which was greater than those (0.66 eV and 0.96 eV) for the Bi (0.96) and Bi (1.00) (Fig. 5c and S21), indicating significant inhibition for the H_2 formation on the Bi (012) surface in presence of strain effects of 6 %. Thus, the strain effects of 6 % decreased the activation energy barrier in the first protonation of CO_2, while significantly improving the HER energy barrier, indicating a more favorable reaction pathway to produce HCOO* rather than *H. To further examine the electron mutual effect of Bi atoms and HCOO* adsorbates, the projected density of state of the d-orbital electron on the Bi atom surface was analyzed (Fig. 5d). Accordingly, strong peak intensity was observed in the d-band center, which is employed to describe the binding strengths of the active sites and adsorbates [40,63]. Furthermore, a stronger peak intensity was observed for HCOO* adsorbed on Bi (1.06), which could be attributed to the stronger bonding between Bi and HCOO* . In addition, volume slices of calculated charge densities for the three models with HCOO* adsorbate were performed; the color bar on the right of Fig. 5e represents the electron cloud density of the model in e/bohr^3. This result represented the strongest electronic density interaction for Bi (1.06). Hence, strain effects play a key role in the HCOO* formation for D-Bi HF.

4. Conclusions

Herein, a large step on hollow-fiber Bi has been achieved in this work to further design lattice-dislocated defect by the in situ electrochemical redox. As-obtained D-Bi HF with the dislocated lattice induced by the strain effect showed a remarkable CO_2RR performance. That is a nearly perfect formate Faradaic efficiency of > 99.5 % was realized with a current density of 1 A cm^{-2}. The COMSOL Multiphysics®-based finite element analysis revealed that the D-Bi HF HPE achieved sufficient CO_2 feeding at triphasic interfaces and promoted CO_2 reduction reaction kinetics under large current density. Moreover, the DFT results demonstrated that the D-Bi with strain effects of 6 % suppressed the HER and simultaneously boosted the eCO_2RR to afford formate. The synergistic combination of the two advantages affords for the superior eCO_2RR performance. This study exhibits great potential for substantial enhancement in the electrocatalytic performance of CO_2 reduction by applying a rational HPE design.

CRediT authorship contribution statement

Aohui Chen: Experiments, Data curation, Writing – original draft. **Chang Zhu:** Data curation. **Jianing Mao:** Experiments, Data curation. **Shoujie Li:** Data curation. **Gangfeng Wu:** Data curation. **Yiheng Wei:** Data curation. **Xiaohu Liu:** Data curation. **Xiao Dong:** Experiments, Data curation. **Yanfang Song:** Data curation. **Guihua Li:** Data curation. **Yuhan Sun:** Supervision. **Wei Wei:** Supervision. **Wei Chen:** Conceptualization, Data curation, Writing – review & editing, Supervision.

Declaration of Competing Interest

The authors declare that they have no known competing financial interests or personal relationships that could have appeared to influence the work reported in this paper.
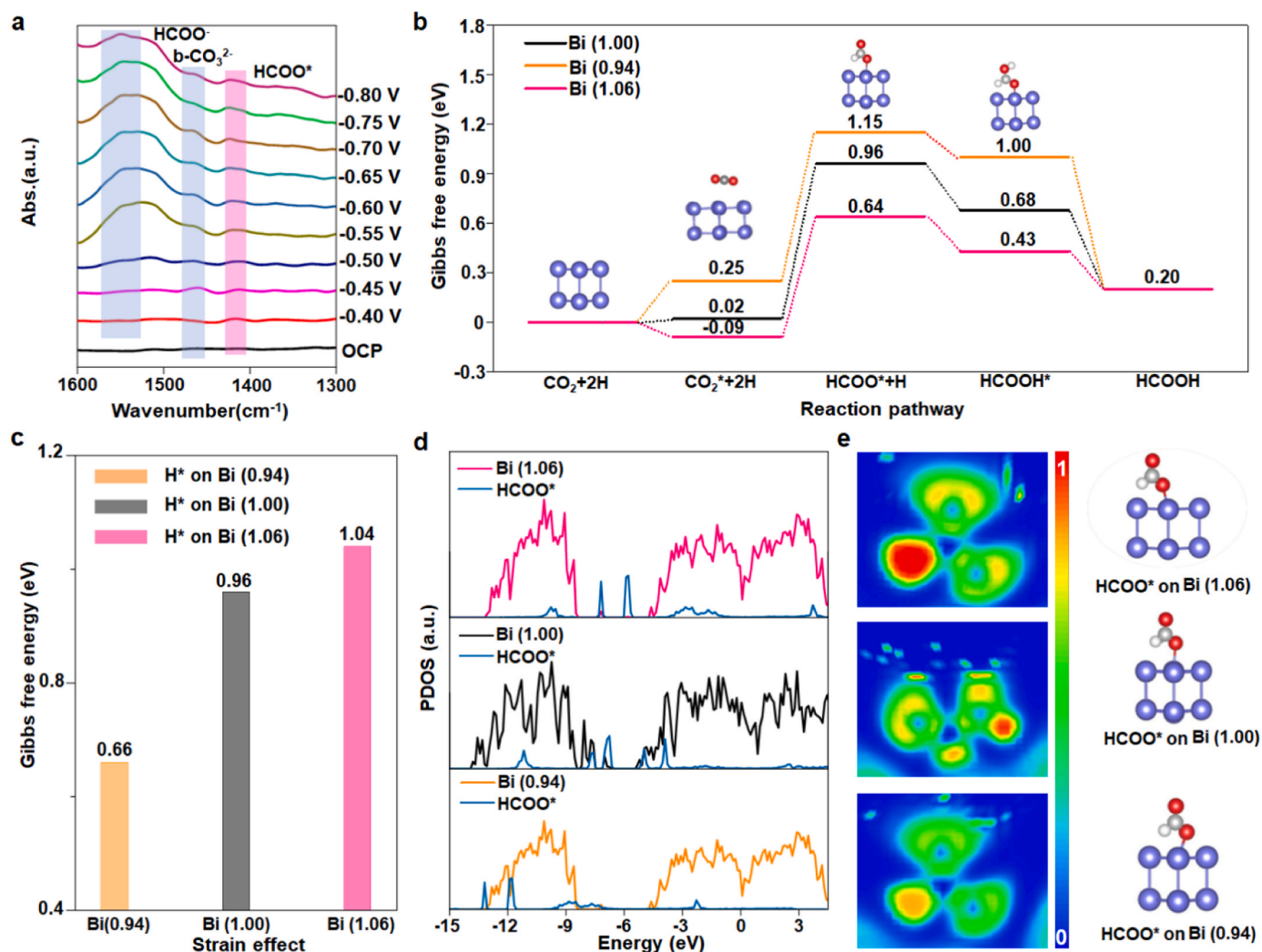
Fig. 5. DFT simulations and proposed catalytic mechanism. (a) ATR-FTIR spectra of D-Bi HF at various applied potentials. (b) Calculated free energy change diagram for CO_2 reduction to HCOOH. (c) Free-energy profiles for H_2 productions. (d) PDOS profiles of surface Bi atoms and HCOO* . (e) Calculated volume slices of calculated charge densities and corresponding optimized configurations for the three models with HCOO* adsorbate under different strain effects.

Data availability

Data will be made available on request.

Appendix A. Supporting information

Supplementary data associated with this article can be found in the online version at doi:10.1016/j.apcatb.2023.123493.

References

[1] S. Mallapaty, How China could be carbon neutral by mid-century, Nature 586 (2020) 482–483.
[2] T. Zheng, M. Zhang, L. Wu, S. Guo, X. Liu, J. Zhao, W. Xue, J. Li, C. Liu, X. Li, Q. Jiang, J. Bao, J. Zeng, T. Yu, C. Xia, Upcycling CO_2 into energy-rich long-chain compounds via electrochemical and metabolic engineering, Nat. Catal. 5 (2022) 388–396.
[3] S.M. Jordaan, C. Wang, Electrocatalytic conversion of carbon dioxide for the Paris goals, Nat. Catal. 4 (2021) 915–920.
[4] X. Zhou, J. Shan, L. Chen, B.Y. Xia, T. Ling, J. Duan, Y. Jiao, Y. Zheng, S.-Z. Qiao, Stabilizing Cu^{2+} ions by solid solutions to promote CO_2 electroreduction to methane, J. Am. Chem. Soc. 144 (2022) 2079–2084.
[5] J. Gu, C.-S. Hsu, L. Bai, H.M. Chen, X. Hu, Atomically dispersed Fe^{3+} sites catalyze efficient CO_2 electroreduction to CO, Science 364 (2019) 1091–1094.
[6] Y. Wu, Z. Jiang, X. Lu, Y. Liang, H. Wang, Domino electroreduction of CO_2 to methanol on a molecular catalyst, Nature 575 (2019) 639–642.
[7] C. Xia, P. Zhu, Q. Jiang, Y. Pan, W. Liang, E. Stavitski, H.N. Alshareef, H. Wang, Continuous production of pure liquid fuel solutions via electrocatalytic CO_2 reduction using solid-electrolyte devices, Nat. Energy 4 (2019) 776–785.
[8] H. Xu, D. Rebollar, H. He, L. Chong, Y. Liu, C. Liu, C.-J. Sun, T. Li, J.V. Muntean, R. E. Winans, D.-J. Liu, T. Xu, Highly selective electrocatalytic CO_2 reduction to ethanol by metallic clusters dynamically formed from atomically dispersed copper, Nat. Energy 5 (2020) 623–632.

[9] J. Jin, J. Wicks, Q. Min, J. Li, Y. Hu, J. Ma, Y. Wang, Z. Jiang, Y. Xu, R. Lu, G. Si, P. Papangelakis, M. Shakouri, Q. Xiao, P. Ou, X. Wang, Z. Chen, W. Zhang, K. Yu, J. Song, X. Jiang, P. Qiu, Y. Lou, D. Wu, Y. Mao, A. Ozden, C. Wang, B.Y. Xia, X. Hu, V.P. Dravid, Y.-M. Yiu, T.-K. Sham, Z. Wang, D. Sinton, L. Mai, E.H. Sargent, Y. Pang, Constrained C_2 adsorbate orientation enables CO-to-acetate electroreduction, Nature 617 (2023) 724–729.

[10] F.P.G. de Arquer, C.T. Dinh, A. Ozden, J. Wicks, C. McCallum, A.R. Kirmani, D. H. Nam, C. Gabardo, A. Seifitokaldani, X. Wang, Y.G.C. Li, F.W. Li, J. Edwards, L. J. Richter, S.J. Thorpe, D. Sinton, E.H. Sargent, CO_2 electrolysis to multicarbon products at activities greater than 1 A cm^{-2}, Science 367 (2020) 661–666.

[11] W. Ma, S. Xie, T. Liu, Q. Fan, J. Ye, F. Sun, Z. Jiang, Q. Zhang, J. Cheng, Y. Wang, Electrocatalytic reduction of CO_2 to ethylene and ethanol through hydrogen-assisted C–C coupling over fluorine-modified copper, Nat. Catal. 3 (2020) 478–487.

[12] R.I. Masel, Z. Liu, H. Yang, J.J. Kaczur, D. Carrillo, S. Ren, D. Salvatore, C. P. Berlinguette, An industrial perspective on catalysts for low-temperature CO_2 electrolysis, Nat. Nanotechnol. 16 (2021) 118–128.

[13] Q. Gong, P. Ding, M. Xu, X. Zhu, M. Wang, J. Deng, Q. Ma, N. Han, Y. Zhu, J. Lu, Z. Feng, Y. Li, W. Zhou, Y. Li, Structural defects on converted bismuth oxide nanotubes enable highly active electrocatalysis of carbon dioxide reduction, Nat. Commun. 10 (2019) 2807.

[14] O.S. Bushuyev, P. De Luna, C.T. Dinh, L. Tao, G. Saur, J. Van De Lagemaat, S. O. Kelley, E.H. Sargent, What should we make with CO_2 and how can we make it? Joule 2 (2018) 825–832.

[15] S. Nitopi, E. Bertheussen, S.B. Scott, X. Liu, A.K. Engstfeld, S. Horch, B. Seger, I.E. L. Stephens, K. Chan, C. Hahn, J.K. Norskov, T.F. Jaramillo, I. Chorkendorff, Progress and perspectives of electrochemical CO_2 reduction on copper in aqueous electrolyte, Chem. Rev. 119 (2019) 7610–7672.

[16] S. Yan, C. Peng, C. Yang, Y. Chen, J. Zhang, A. Guan, X. Lv, H. Wang, Z. Wang, T. K. Sham, Q. Han, G. Zheng, Electron localization and lattice strain induced by surface lithium doping enable ampere-level electrosynthesis of formate from CO_2, Angew. Chem. Int. Ed. 60 (2021) 25741–25745.

[17] Y. Xiong, J. Dong, Z.-Q. Huang, P. Xin, W. Chen, Y. Wang, Z. Li, Z. Jin, W. Xing, Z. Zhuang, J. Ye, X. Wei, R. Cao, L. Gu, S. Sun, L. Zhuang, X. Chen, H. Yang, C. Chen, Q. Peng, C.-R. Chang, D. Wang, Y. Li, Single-atom Rh/N-doped carbon electrocatalyst for formic acid oxidation, Nat. Nanotechnol. 15 (2020) 390–397.

[18] Z. Li, A. Cao, Q. Zheng, Y. Fu, T. Wang, K.T. Arul, J.-L. Chen, B. Yang, N.M. Adli, L. Lei, C.-L. Dong, J. Xiao, G. Wu, Y. Hou, Elucidation of the synergistic effect of dopants and vacancies on promoted selectivity for CO_2 electroreduction to formate, Adv. Mater. 33 (2021), 2005113.

[19] L. Xiao, X. Liu, R. Zhou, T. Zhang, R. Zhou, B. Ouyang, E. Kan, P.J. Cullen, K. Ostrikov, X. Tu, Facile synthesis of high-performance indium nanocrystals for selective CO_2-to-formate electroreduction, Energy Convers. Manag. 231 (2021), 113847.

[20] N. Zouaoui, B.D. Ossonon, M. Fan, D. Mayilukila, S. Garbarino, G. de Silveira, G. A. Botton, D. Guay, A.C. Tavares, Electroreduction of CO_2 to formate on amine modified Pb electrodes, J. Mater. Chem. A 7 (2019) 11272–11281.

[21] H. Zhong, Y. Qiu, T. Zhang, X. Li, H. Zhang, X. Chen, Bismuth nanodendrites as a high performance electrocatalyst for selective conversion of CO_2 to formate, J. Mater. Chem. A 4 (2016) 13746–13753.

[22] L. Lv, R. Lu, J. Zhu, R. Yu, W. Zhang, E. Cui, X. Chen, Y. Dai, L. Cui, J. Li, L. Zhou, W. Chen, Z. Wang, L. Mai, Coordinating the edge defects of bismuth with sulfur for enhanced CO_2 electroreduction to formate, Angew. Chem. Int. Ed. 62 (2023), e202303117.

[23] Y. Qiao, W. Lai, K. Huang, T. Yu, Q. Wang, L. Gao, Z. Yang, Z. Ma, T. Sun, M. Liu, C. Lian, H. Huang, Engineering the local microenvironment over Bi nanosheets for highly selective electrocatalytic conversion of CO_2 to HCOOH in strong acid, ACS Catal. 12 (2022) 2357–2364.

[24] Y. Li, J. Chen, S. Chen, X. Liao, T. Zhao, F. Cheng, H. Wang, In Situ confined growth of bismuth nanoribbons with active and robust edge sites for boosted CO_2 electroreduction, ACS Energy Lett. 7 (2022) 1454–1461.

[25] M. Zhang, W. Wei, S. Zhou, D.-D. Ma, A. Cao, X.-T. Wu, Q.-L. Zhu, Engineering a conductive network of atomically thin bismuthene with rich defects enables CO_2 reduction to formate with industry-compatible current densities and stability, Energy Environ. Sci. 14 (2021) 4998–5008.

[26] Z. Xing, X. Hu, X. Feng, Tuning the microenvironment in gas-diffusion electrodes enables high-rate CO_2 electrolysis to formate, ACS Energy Lett. 6 (2021) 1694–1702.

[27] N. Han, Y. Wang, H. Yang, J. Deng, J. Wu, Y. Li, Y. Li, Ultrathin bismuth nanosheets from in situ topotactic transformation for selective electrocatalytic CO_2 reduction to formate, Nat. Commun. 9 (2018) 1320.

[28] H. Yang, N. Han, J. Deng, J. Wu, Y. Wang, Y. Hu, P. Ding, Y. Li, Y. Li, J. Lu, Selective CO_2 reduction on 2D mesoporous Bi nanosheets, Adv. Energy Mater. 8 (2018), 1801536.

[29] F. Yang, A.O. Elnabawy, R. Schimmenti, P. Song, J. Wang, Z. Peng, S. Yao, R. Deng, S. Song, Y. Lin, M. Mavrikakis, W. Xu, Bismuthene for highly efficient carbon dioxide electroreduction reaction, Nat. Commun. 11 (2020) 1088.

[30] H. Rabiee, L. Ge, X. Zhang, S. Hu, M. Li, Z. Yuan, Gas diffusion electrodes (GDEs) for electrochemical reduction of carbon dioxide, carbon monoxide, and dinitrogen to value-added products: a review, Energy Environ. Sci. 14 (2021) 1959–2008.

[31] L. Lin, X. He, X.G. Zhang, W. Ma, B. Zhang, D. Wei, S. Xie, Q. Zhang, X. Yi, Y. Wang, A nanocomposite of bismuth clusters and Bi $_2O_3$ sheets for highly efficient electrocatalytic reduction of CO_2, Angew. Chem. Int. Ed. 62 (2023), 202214959.

[32] A. Chen, X. Dong, J. Mao, W. Chen, C. Zhu, S. Li, G. Wu, Y. Wei, X. Liu, G. Li, Y. Song, Z. Jiang, W. Wei, Y. Sun, Gas penetrating hollow fiber Bi with contractive bond enables industry-level CO_2 electroreduction, Appl. Catal. B Environ. 333 (2023), 122768.

[33] R. Kas, K.K. Hummadi, R. Kortlever, P. de Wit, A. Milbrat, M.W. Luiten-Olieman, N. E. Benes, M.T. Koper, G. Mul, Three-dimensional porous hollow fibre copper electrodes for efficient and high-rate electrochemical carbon dioxide reduction, Nat. Commun. 7 (2016) 10748.

[34] B. Chen, J. Xu, J. Zou, D. Liu, Y. Situ, H. Huang, Formate-selective CO_2 electrochemical reduction with a hydrogen reduction suppressing bronze alloy hollow-fiber electrode, ChemSusChem 13 (2020) 6594–6601.

[35] H. Rabiee, L. Ge, X. Zhang, S. Hu, M. Li, S. Smart, Z. Zhu, Z. Yuan, Shape-tuned electrodeposition of bismuth-based nanosheets on flow-through hollow fiber gas diffusion electrode for high-efficiency CO_2 reduction to formate, Appl. Catal. B Environ. 286 (2021), 119945.

[36] C. Zhu, G. Shen, W. Chen, X. Dong, G. Li, Y. Song, Y. Wei, Y. Sun, Copper hollow fiber electrode for efficient CO_2 electroreduction, J. Power Sources 495 (2021), 229814.

[37] Y. Song, X. Dong, W. Chen, W. Wei, Hollow-fiber gas penetration electrodes efficiently produce renewable synthetic fuels, Front. Energy 16 (2022) 700–705.

[38] L. Yi, J. Chen, P. Shao, J. Huang, X. Peng, J. Li, G. Wang, C. Zhang, Z. Wen, Molten-salt-assisted synthesis of bismuth nanosheets for long-term continuous electrocatalytic conversion of CO_2 to formate, Angew. Chem. Int. Ed. 59 (2020) 20112–20119.

[39] S. He, F. Ni, Y. Ji, L. Wang, Y. Wen, H. Bai, G. Liu, Y. Zhang, Y. Li, B. Zhang, H. Peng, The p-orbital delocalization of main-group metals to boost CO_2 electroreduction, Angew. Chem. Int. Ed. 57 (2018) 16114–16119.

[40] B. Ren, G. Wen, R. Gao, D. Luo, Z. Zhang, W. Qiu, Q. Ma, X. Wang, Y. Cui, L. Ricardez–Sandoval, A. Yu, Z. Chen, Nano-crumples induced Sn-Bi bimetallic interface pattern with moderate electron bank for highly efficient CO_2 electroreduction, Nat. Commun. 13 (2022) 2486.

[41] Y. Hu, D. Lu, W. Zhou, X. Wang, Y. Li, In situ construction of 3D low-coordinated bismuth nanosheets@Cu nanowire core–shell nanoarchitectures for superior CO_2 electroreduction activity, J. Mater. Chem. A 11 (2023) 1937–1943.

[42] S. Li, W. Chen, X. Dong, C. Zhu, A. Chen, Y. Song, G. Li, W. Wei, Y. Sun, Hierarchical micro/nanostructured silver hollow fiber boosts electroreduction of carbon dioxide, Nat. Commun. 13 (2022) 3080.

[43] S. Li, X. Dong, Y. Zhao, J. Mao, W. Chen, A. Chen, Y. Song, G. Li, Z. Jiang, W. Wei, Y. Sun, Chloride ion adsorption enables ampere-level CO_2 electroreduction over silver hollow fiber, Angew. Chem. Int. Ed. 61 (2022), e202210432.

[44] C. Zhu, Y. Song, X. Dong, G. Li, A. Chen, W. Chen, G. Wu, S. Li, W. Wei, Y. Sun, Ampere-level CO_2 reduction to multicarbon products over a copper gas penetration electrode, Energy Environ. Sci. 15 (2022) 5391–5404.

[45] A. Dutta, I. Zelocualtecatl Montiel, K. Kiran, A. Rieder, V. Grozovski, L. Gut, P. Broekmann, A tandem (Bi_2O_3→Bimet) catalyst for highly efficient ec-CO_2 conversion into formate: Operando Raman spectroscopic evidence for a reaction pathway change, ACS Catal. 11 (2021) 4988–5003.

[46] X. Zhang, X. Sun, S.-X. Guo, A.M. Bond, J. Zhang, Formation of lattice-dislocated bismuth nanowires on copper foam for enhanced electrocatalytic CO_2 reduction at low overpotential, Energy Environ. Sci. 12 (2019) 1334–1340.

[47] S. Liu, Y. Shen, Y. Zhang, B. Cui, S. Xi, J. Zhang, L. Xu, S. Zhu, Y. Chen, Y. Deng, W. Hu, Extreme environmental thermal shock induced dislocation-rich Pt nanoparticles boosting hydrogen evolution reaction, Adv. Mater. 34 (2022), 2106973.

[48] B. Qin, Q. Zhang, Y.-H. Li, G. Yang, F. Peng, Formation of lattice-dislocated zinc oxide via anodic corrosion for electrocatalytic CO_2 reduction to syngas with a potentialdependent CO:H2 ratio, ACS Appl. Mater. Interfaces 12 (2020) 30466–30473.

[49] Y. Wang, Y. Gong, Y. Wang, L. Gao, Lattice-dislocated Bi nanosheets for electrocatalytic reduction of carbon dioxide to formate over a wide potential window, J. Colloid Interface Sci. (611) (2022) 246–254.

[50] P.P. Yang, X.L. Zhang, P. Liu, D.J. Kelly, Z.Z. Niu, Y. Kong, L. Shi, Y.R. Zheng, M. H. Fan, H.J. Wang, M.R. Gao, Highly enhanced chloride adsorption mediates efficient neutral CO_2 electroreduction over a dual-phase copper catalyst, J. Am. Chem. Soc. 145 (2023) 8714–8725.

[51] J. Fan, X. Zhao, X. Mao, J. Xu, N. Han, H. Yang, B. Pan, Y. Li, L. Wang, Y. Li, Large-area vertically aligned bismuthene nanosheet arrays from galvanic replacement reaction for efficient electrochemical CO_2 conversion, Adv. Mater. 33 (2021), 2100910.

[52] Y. Hu, X. Wang, J. Zhang, J. Zhang, Y. Zhang, J. Liang, Y. Li, In situ engineering 3D conductive core-shell nano-networks and electronic structure of bismuth alloy nanosheets for efficient electrocatalytic CO_2 reduction, Sci. China Mater. 66 (2023) 2266–2273.

[53] B. Zhang, J. Shan, X. Wang, Y. Hu, Y. Li, Ru/Rh cation doping and oxygenvacancy engineering of FeOOH Nanoarrays@Ti3C2Tx MXene heterojunction for highly efficient and stable electrocatalytic oxygen evolution, Small 18 (2022), e2200173.

[54] B. Zhang, J. Shan, W. Wang, P. Tsiakaras, Y. Li, Oxygen vacancy and core–shell heterojunction engineering of anemone-like CoP@CoOOH bifunctional electrocatalyst for efficient overall water splitting, Small 18 (2022), 2106012.

[55] C. Yan, H. Li, Y. Ye, H. Wu, F. Cai, R. Si, J. Xiao, S. Miao, S. Xie, F. Yang, Y. Li, G. Wang, X. Bao, Coordinatively unsaturated nickel–nitrogen sites towards selective and high-rate CO_2 electroreduction, Energy Environ. Sci. 11 (2018) 1204–1210.

[56] T. Burdyny, P.J. Graham, Y. Pang, C.-T. Dinh, M. Liu, E.H. Sargent, D. Sinton, Nanomorphology-enhanced gas-evolution intensifies CO_2 reduction electrochemistry, ACS Sustain. Chem. Eng. 5 (2017) 4031–4040.

[57] T. Burdyny, W.A. Smith, CO_2 reduction on gas-diffusion electrodes and why catalytic performance must be assessed at commercially-relevant conditions, Energy Environ. Sci. 12 (2019) 1442–1453.

[58] D.M. Weekes, D.A. Salvatore, A. Reyes, A. Huang, C.P. Berlinguette, Electrolytic CO_2 reduction in a flow cell, Acc. Chem. Res. 51 (2018) 910–918.

[59] Z. Wu, H. Wu, W. Cai, Z. Wen, B. Jia, L. Wang, W. Jin, T. Ma, Engineering bismuth–tin interface in bimetallic aerogel with a 3D porous structure for highly selective electrocatalytic CO_2 reduction to HCOOH, Angew. Chem. Int. Ed. 60 (2021) 12554–12559.

[60] Q. Wang, X. Yang, H. Zang, C. Liu, J. Wang, N. Yu, L. Kuai, Q. Qin, B. Geng, InBi bimetallic sites for efficient electrochemical reduction of CO_2 to HCOOH, Small (2023), 2303172.

[61] R. Zhang, H. Wang, S. Tang, C. Liu, F. Dong, H. Yue, B. Liang, Photocatalytic oxidative dehydrogenation of ethane using CO_2 as a soft oxidant over Pd/TiO_2 catalysts to C_2H_4 and syngas, ACS Catal. 8 (2018) 9280–9286.

[62] A. Solis-Garcia, J.F. Louvier-Hernandez, A. Almendarez-Camarillo, J.C. Fierro-Gonzalez, Participation of surface bicarbonate, formate and methoxy species in the carbon dioxide methanation catalyzed by ZrO_2-supported Ni, Appl. Catal. B Environ. 218 (2017) 611.

[63] B. Ren, X. Dong, Y. Yu, G. Wen, M. Zhang, A density functional theory study on the carbon chain growth of ethanol formation on Cu-Co (111) and (211) surfaces, Appl. Surf. Sci. 412 (2017) 374–384.